ACS APPLIED MATERIALS & INTERFACES

www.acsami.org

Research Article

Paraffin-Enabled Compressive Folding of Two-Dimensional Materials with Controllable Broadening of the Electronic Band Gap

Weifeng Zhang,[‖] Zihan Zhao,[‖] Yating Yang, Yan Zhang, He Hao, Li Li, Weigao Xu, Banghua Peng, Run Long, and Nan Liu*

Cite This: *ACS Appl. Mater. Interfaces* 2021, 13, 40922−40931

Read Online

ACCESS | Metrics & More | Article Recommendations | Supporting Information

ABSTRACT: The capability to manipulate the size of the electronic band gap is of importance to semiconductor technology. Among these, a wide direct band gap is particularly helpful in optoelectronic devices due to the efficient utilization of blue and ultraviolet light. Here, we reported a paraffin-enabled compressive folding (PCF) strategy to widen the band gap of two-dimensional (2D) materials. Due to the large thermal expansion coefficient of paraffin, folded 2D materials can be achieved via thermal engineering of the paraffin-assisted transfer process. It can controllably introduce 0.2−1.3% compressive strain onto folded structures depending on the temperature differences and transfer the folding product to both rigid and soft substrates. Exemplified by MoS_2, its folded multilayers demonstrated blue-shifts at direct gap transition peaks, six times stronger photoluminescence intensity, almost double mobility, and 20 times higher photoresponsivity over unfolded MoS_2. This PCF strategy can attain controllable widening band gap of 2D materials, which will open up novel applications in optoelectronics.

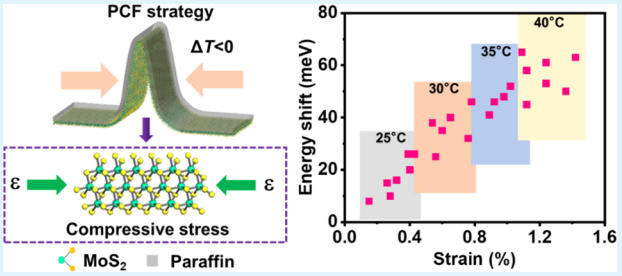

KEYWORDS: *compressive strain, folding, 2D materials, paraffin, broadening band gap*

INTRODUCTION

Band gap tuning is a main goal in exploring two-dimensional (2D) materials[1] because they exhibit distinct electronic band gap structures for diverse applications, such as photodetectors,[2,3] light-emitting diodes,[4] catalysis,[5] and energy storage and conversion devices.[6,7] To synthesize various types of 2D materials in high quality and controllable fashion, it requires tremendous efforts in chemical vapor deposition (CVD) growth, including optimizing experimental setups, raw materials, growth substrates, and so on.[8] Chemical,[9] ion-implant,[10] and electrostatic doping[11] are excellent in tuning charge carrier density, but they lack in continuous band gap tailoring and often change the original structure of 2D materials. Therefore, a method to tune band gap of 2D materials rather than synthesis and doping is desirable.

Topology engineering such as making wrinkles and folds on 2D materials was predicted to tune band gap efficiently in theory.[12,13] For example, due to weak interlayer coupling in adjacent layers, multilayer MoS_2 folded or wrinkled from the monolayer exhibits direct gap transition with increased light absorption, which will be beneficial to optoelectronic devices.[14,15] However, in the experiment, fabrication of wrinkles/folds has been mostly achieved on graphene,[16−19] and there were only a few reports available on transition-metal dichalcogenides (TMDs), in particular on large-scale CVD-grown TMDs. Based on exfoliated MoS_2, wrinkles and folds were obtained by releasing the pre-stretched substrate[14,20−24] and heating substrate,[22,23] and some some wrinkles and folds may also form during the transfer process.[25] Band gap tuning by these methods is restricted in red-shift of band gap originated from tensile stress. Applying compressive stress on MoS_2 using the electromechanical device was reported to induce blue-shift of direct band gap,[26] but this method relied on complicated controlling circuits and the compressive stress would vanish once the electricity was off. Therefore, a long-lasting and controllable method to introduce compressive stress for a wider band gap on CVD TMDs is urgently needed.

Semiconductive TMDs mostly possess electronic band gaps below 1.80 eV.[27] A wider band gap is particularly useful in optoelectronic devices such as light-emitting diodes,[28−30] field effect transistors (FETs),[31−33] and photodetectors[34,35] because they are crucial in suppressing tunneling from source to drain electrodes, leading to larger on/off ratio and higher mobility. Moreover, semiconductor with wider band gap absorbs blue and ultraviolet light with high energy. Together with folding up TMDs, which can increase light absorption and maintain direct

Received: June 16, 2021
Accepted: August 9, 2021
Published: August 19, 2021

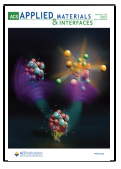

https://doi.org/10.1021/acsami.1c11269
ACS Appl. Mater. Interfaces 2021, 13, 40922−40931

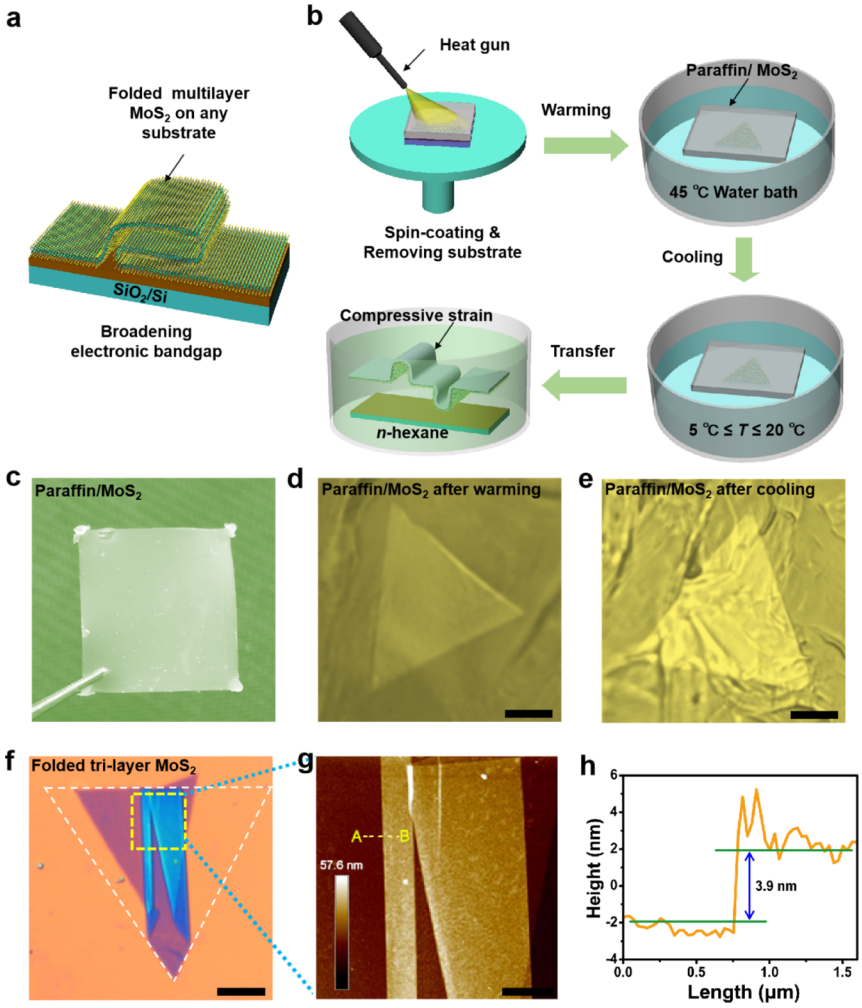

Figure 1. Strategy of PCF for MoS_2. (a,b) Schematic illustration of the fabrication process of folded multilayer MoS_2 by PCF. It involves the spin-coating paraffin layer onto the $MoS_2/SiO_2/Si$ substrate, releasing the paraffin/MoS_2 film, warming and cooling of the paraffin/MoS_2 film, transferring it onto the target substrate, and dissolving paraffin by *n*-hexane. Folded multilayer MoS_2 can be achieved on any substrate with broadening electronic band gap. (c) Photograph of the paraffin/MoS_2 film. (d,e) Optical microscopy images of the paraffin/MoS_2 film after (d) warming and (e) cooling, showing absence and occurrence of wrinkles by thermal engineering. (f) Optical microscopy image of folded tri-layer MoS_2 on a SiO_2/Si substrate by PCF. (g) AFM image of the square region in (f). (h) Height profile along the dashed line in (f). The white wire frame is monolayer MoS_2 before folding. Scale bars, 5 μm.

gap transition, compressive folding of TMDs is of great potential in enhancing optoelectronic performances.

Here, we presented a paraffin-enabled compressive folding (PCF) strategy to acquire broadening band gap of 2D materials in a long-lasting and controllable way. Exemplified by MoS_2 grown by CVD, folded multilayers can be obtained via thermal engineering of paraffin carrier layer during transfer and demonstrated abnormal blue-shifts in peaks and increases in intensity by Raman and photoluminescence (PL) spectroscopy compared to most topology engineering. By controlling the temperature differences during PCF, it can controllably introduce 0.2−1.3% compressive strain, leading to folded structures with controllable band gap increase on any (rigid and elastic) substrate. This immediately allowed fabrication of FETs and photodetectors with improved performances, such as higher mobility and photoresponsivity. Moreover, broadening electronic band gap of MoS_2 by PCF can be extended to various 2D materials. We believe that our PCF strategy offers a universal method to controllably broadening electronic band gap of 2D materials, opening up novel opportunities in optoelectronics (Table S1, Supporting Information).

RESULTS AND DISCUSSION

Strategy of PCF. We exemplify the PCF process using MoS_2, as illustrated in Figure 1a,b. First, the liquid paraffin (>80 °C) was spin-coated on CVD-grown MoS_2 on a SiO_2/Si substrate. To maintain paraffin at liquid status for entire coverage on the substrate and to control paraffin thickness more accurately, heat gun was blown during spin-coating. The paraffin/MoS_2 film was then released by etching off an underlying SiO_2/Si substrate in KOH aq. at 45 °C, followed by cleaning up residual KOH in deionized water (Figure 1c). Subsequently, the self-supported film was frozen at 5 °C (10, 15, and 20 °C) for 24 h and transferred onto a target substrate with natural drying at the same temperature. Before cooling, the paraffin/MoS_2 film showed a smooth surface without fold on MoS_2 under an optical microscope (Figure 1d), and at freezing, MoS_2 would be "pulled up" due to the shrinkage of paraffin, giving rise to fold over the entire paraffin/MoS_2 film

https://doi.org/10.1021/acsami.1c11269
ACS Appl. Mater. Interfaces 2021, 13, 40922−40931

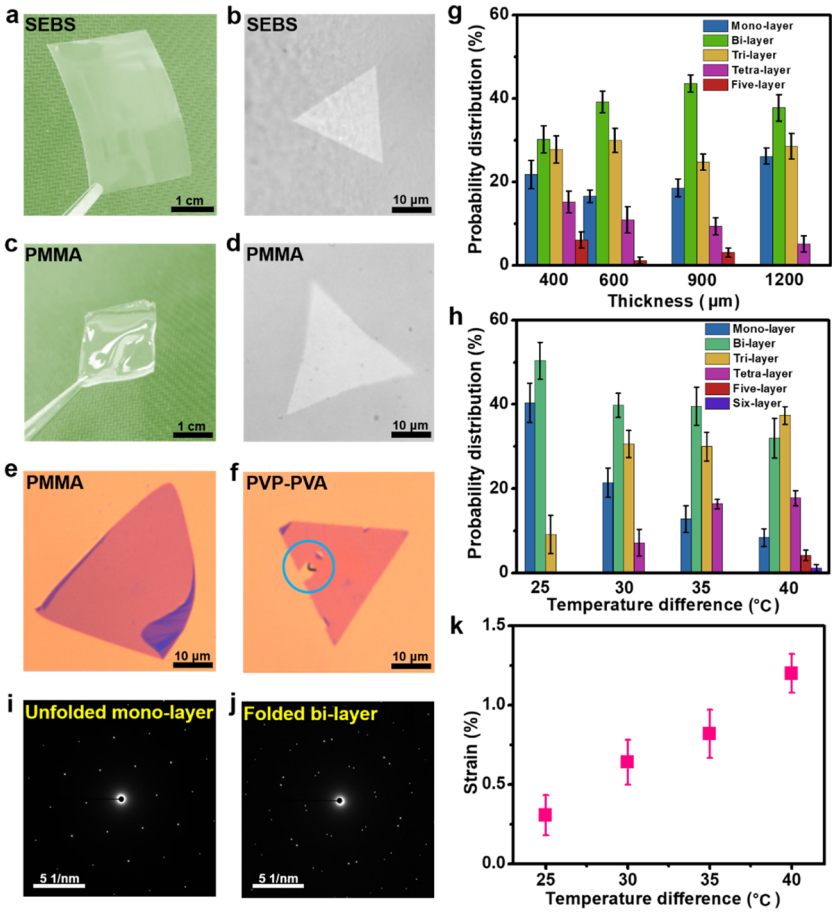

Figure 2. Uniqueness of paraffin in compressive folding. (a–d) Photographs and optical microscopy images of (a,b) SEBS/MoS_2 and (c,d) PMMA/MoS_2 films through the same thermal engineering as that by paraffin. (e,f) Optical microscopy images of (e) PMMA- and (f) PVA-PVP-assisted transferred MoS_2 on SiO_2/Si substrates. (g,h) Statistical histograms of probability distribution (P_i) of each layer number (i-layer) of MoS_2 films after the PCF strategy at various (g) thicknesses of paraffin films and (h) temperature differences of thermal engineering processes. (i,j) SAED patterns of unfolded monolayer MoS_2 and folded bilayer MoS_2 formed at a temperature difference of 40 °C. (k) Dependence of compressive strain as a function of temperature differences during PCF.

(Figure 1e). As the paraffin had an excellent solubility in *n*-hexane, folded MoS_2 by PCF demonstrated a very clean surface, such as on a SiO_2/Si substrate (Figure 1f). Characterized by atomic force microscopy (AFM) and scanning electron microscopy (SEM) (Figures 1g,h and S1, Supporting Information), the height of folded tri-layer MoS_2 was as large as ∼4 nm, which suggested a very weak interlayer coupling. It is worth noting that the PCF strategy is advantageous in directly transferring folded MoS_2 onto rigid substrates (e.g., Al_2O_3, mica, and Na_2SiO_3 glass) and elastic substrates (e.g., PDMS) over other strain engineering methods[12,36] (Figure S2, Supporting Information). In addition, folded graphene, boron nitride (BN), and $MoSe_2$ were successfully achieved on SiO_2/Si substrates under the same conditions of PCF processing, further demonstrating the universality of the PCF strategy (Figure S3, Supporting Information). We hypothesized that temperature perturbation on the paraffin film brings compressive stress on MoS_2 and led to the folding of MoS_2. The thermal engineering evolution was simulated via the finite element method (Figure S4, Supporting Information).

Uniqueness of Paraffin and Quantification of Strain in Compressive Folding. Paraffin plays a critical role in this compressive folding process. The reason we chose the paraffin as an assisted folding layer is its large thermal expansion coefficient (7.6×10^{-4}/°C) and low melting point (45 °C).[37,38] With these two characteristics, the paraffin can introduce sufficiently large compressive stress for band gap tuning by mediating temperature, and its morphology can be readily manipulated as it is soft at room temperature. We also performed the same temperature disturbance investigation on various polymers. Polystyrene-*b*-poly (ethylene-*co*-butylene)-*b*-polystyrene (SEBS) is often used as an elastomer substrate in stretchable electronics, whose thermal expansion coefficient (1.6×10^{-4}/°C) is about four times lower than paraffin. SEBS held MoS_2 at the same thickness with paraffin was flat after experiencing the same heating–cooling process (Figure 2a). No crumpled region was observed on MoS_2/SEBS under an optical microscope (Figure 2b). Similar results can be observed using polymethyl methacrylate (PMMA) at the same conditions (Figure 2c,d), which is also attributed to the low thermal expansion coefficient of PMMA (2.1×10^{-4}/°C).[39] In addition, PMMA and polyvinyl alcohol (PVA)/polyvinyl-pyrrolidone (PVP),[40] as two frequently used transfer layers, were also used to fabricate folded MoS_2 under the same conditions. We indeed occasionally observed folds/wrinkles/cracks, but in most cases, MoS_2 flakes were flat triangles (Figure 2e,f). Also, the folds created by PMMA and PVP–PVA were relatively small compared with those by the paraffin and tended to occur at the edges of MoS_2 accompanied with some

https://doi.org/10.1021/acsami.1c11269
ACS Appl. Mater. Interfaces 2021, 13, 40922–40931

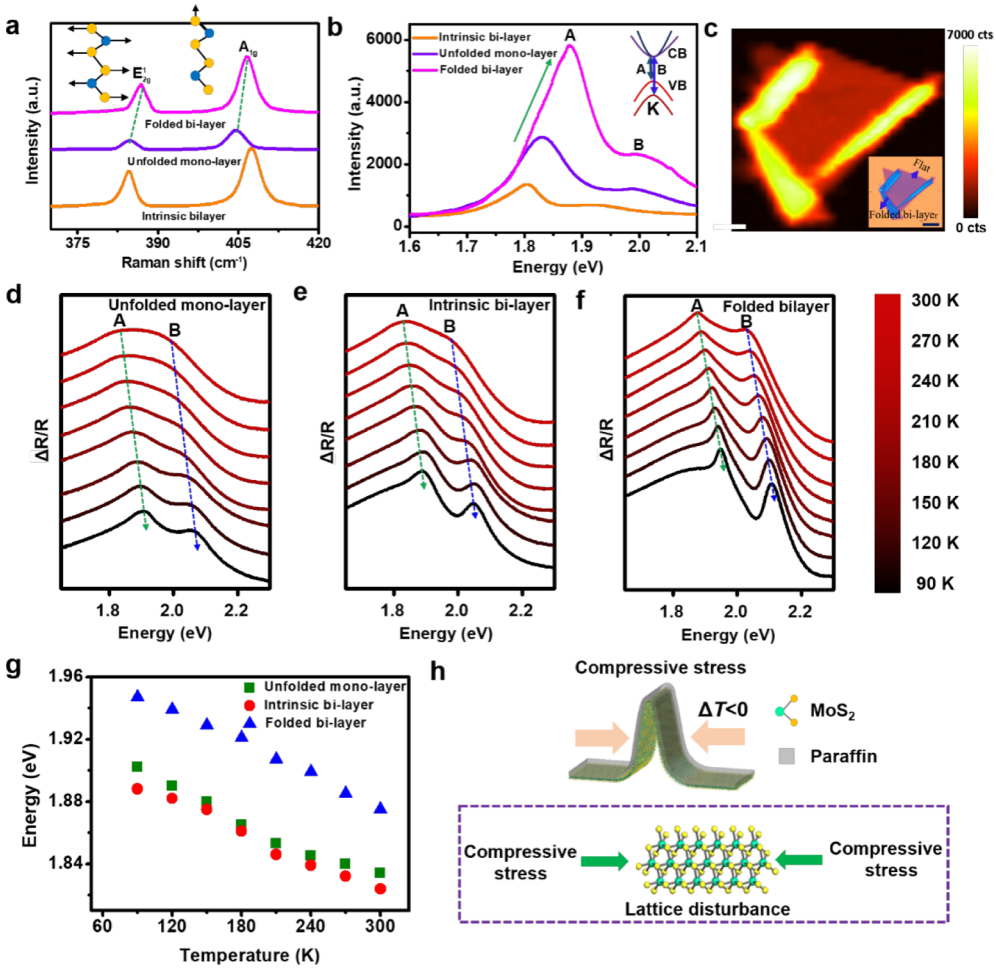

Figure 3. Spectroscopic study on the folded structures by PCF. (a,b) (a) Raman and (b) PL spectra of the folded bilayer (ΔT = 40 °C), unfolded monolayer, and intrinsic bilayer MoS_2. The insets of (a,b) exhibit the vibration modes of characteristic Raman peaks and the radiative recombination path of *A* and *B* excitons in PL. *A* and *B* exciton peaks are two resonances indicative of direct gap transitions resulting from the energy split from spin−orbit coupling of VB to the CB at the *K* point of the Brillouin zone, as depicted in the inset of (b). (c) PL mapping of *A* exciton peak intensity of folded MoS_2. Inset of (c) is the corresponding optical microscopy image of the mapping region. Scale bar, 5 μm. (d−f) Temperature-dependent reflectance contrast spectra for (d) unfolded monolayer, (e) intrinsic bilayer, and (f) folded bilayer MoS_2. (g) Energy of *A* exciton peak for the unfolded monolayer, intrinsic bilayer, and folded bilayer MoS_2 as a function of temperature. (h) Schematic diagram of the compressive stress on folded MoS_2 while cooling the film of paraffin/MoS_2 during PCF.

cracks. In contrast, folded MoS_2 via PCF can be found in the inner plane or at any side of a single crystalline triangle with a large area (Figure S5, Supporting Information).

Folding can be adjustable by paraffin thicknesses and temperature gradients. We compared the formation of folded structures by PCF with different paraffin thicknesses of 400, 600, 900, and 1200 μm and at temperature perturbation differences of 25, 30, 35, and 40 °C (Figure 2g,h). Folded structures form multilayer MoS_2. Layer number of folded structures (i-layer) after PCF was statistically analyzed over 20 areas of 100 × 100 μm at each folding condition (Figure S6, Supporting Information). Probability distribution (P_i) of each layer number can be expressed as

$$P_i = \frac{n_i}{N} \tag{1}$$

where n_i is the total number of *i*-layer folded structures and *N* is the amount of MoS_2 flakes. Note that all MoS_2 flakes prior to PCF are monolayers, and after PCF, monolayers represent unfolded flakes. Statistical histograms show that at thin paraffin thickness and large temperature gradient, more MoS_2 flakes will be folded with thicker folded number. This can be explained by the following formula

$$\frac{\Delta L}{L} = \alpha \Delta T \tag{2}$$

where $\Delta L/L$ denotes morphology change along one direction, α is the linear thermal expansion coefficient, and ΔT is the temperature difference. Due to thermal compression from paraffin, more and thicker folded MoS_2 will be formed at larger temperature gradients. Various paraffin types correspond to thermal expansion coefficients ranging from 0.7 × 10^{-4}/°C to 10.8 × 10^{-4}/°C.[41] Changing paraffin type can effectively tune the strength of compressive stress. Moreover, thinner paraffin will facilitate stress transfer onto underlying MoS_2. We noted that paraffin thinner than 400 μm tended to deform and break during handling, which required an additional assistant layer (Figure S7, Supporting Information). Therefore, our optimized PCF condition is paraffin thickness of 600 μm at the temperature difference of 40 °C, yielding up to 92% folded MoS_2.

https://doi.org/10.1021/acsami.1c11269
ACS Appl. Mater. Interfaces 2021, 13, 40922−40931

We next quantified the strain induced by PCF under different temperature differences (25, 30, 35, and 40 °C) at a fixed paraffin type and thickness. It is reported that strain distorts the intrinsic atomic structure of TMD materials.[1] Thus, we performed and analyzed the selected area electron diffraction (SAED) patterns of folded structures and unfolded monolayers to extract and compare their lattice constants (Figures 2i,j, S8 and S9, Supporting Information). The compressive strain on folded structures can be evaluated via the formula

$$\varepsilon = |(a_2 - a_1)/a_1| \quad (3)$$

where a_1 and a_2 are the lattice constants of unfolded monolayer and folded structures, respectively. Based on 24 statistical data, the compressive strains on folded structures formed under abovementioned temperature differences during PCF were 0.31 ± 0.12%, 0.64 ± 0.14%, 0.82 ± 0.15%, and 1.21 ± 0.12%, respectively (Figure 2k). According to such dependences, we concluded that thermal engineering of paraffin during PCF indeed induced compressive strain on folded structures, and the strain was directly correlated with temperature gradients.

Blue-Shifts in Direct Gap Transitions Using the PCF Strategy. To understand the effects of strain on the structure and gap transitions, we performed systematically spectroscopic study on the folded structures formed at the optimized condition of PCF. Compared with unfolded monolayer MoS_2, folded bilayer by PCF exhibited blue-shifts in characteristic Raman modes of E_{2g}^1 and A_{1g} with much higher intensity (Figures 3a and S10, Supporting Information), which are completely opposite with most changes (red-shifts) using the strain engineering methods.[12,36] This abnormal blue-shift and stiffening indicated compressive strain and accumulation of photons on the folded bilayer using the PCF strategy. Because E_{2g}^1 corresponds to sulfur and molybdenum atoms oscillating in the anti-phase parallel to the crystal plane, under compressive stress, the wavenumber blue-shift of E_{2g}^1 is larger than that of A_{1g}, which corresponds to the sulfur atoms oscillating in the anti-phase out-of-plane. Therefore, the frequency difference between the E_{2g}^1 and the A_{1g} of the folded bilayer (~19.9 cm^{-1}) is smaller than that of the AB stacked bilayer (~21.9 cm^{-1}) and close to the monolayer MoS_2 (~19.6 cm^{-1}). This also indicates a reduced interlayer coupling in the folded bilayer by PCF.[15,42]

PL spectra also showed a prominent blue-shift in A exciton peak with two and six times of intensity on the folded bilayer MoS_2 by PCF than that of the unfolded monolayer and intrinsic bilayer region, respectively (Figure 3b). A exciton peak position and intensity mapping demonstrated an uniform strain distribution over a 60 μm^2 folded region (Figures 3c, S11 and S12, Supporting Information). To verify the folding-induced band gap increasing, we compared the reflectance contrast spectra of the unfolded monolayer, intrinsic bilayer MoS_2, and folded bilayer MoS_2 as a function of temperature (Figure 3d–f).[43,44] At each temperature, both *A* and *B* exciton resonance peaks of folded bilayer MoS_2 shifted to higher energy and exhibit smaller exciton widths than those of unfolded monolayers and intrinsic bilayers (Figure 3g), being consistent with the trend observed at room-temperature PL. With decreasing temperature, *A* and *B* exciton peaks for all these three types of samples present a systematically blue shift, which can be attributed to either the change in the lattice[45] or the polaron effects.[46] The above results for temperature-dependent reflectance contrast spectra suggest that the PCF process enables the direct band gap extension, regardless of activated exciton species and temperature. The band gap blueshift induced via PCF was further verified by the temperature-dependent PL spectra (Figure S13, Supporting Information). This blue-shift trend is in good agreement with the results in temperature-dependent reflectance contrast spectra, further indicating that a broadening of direct band gap can be achieved using the PCF strategy.

The scenario of compressive stress using the PCF strategy versus most scenarios of tensile stress by stretching underlying elastomers was schematically explained and shown (Figures 3h and S14, Supporting Information). Normally, bilayer MoS_2 is an indirect band-gap semiconductor[47] with a much lower PL intensity due to electronic relaxation.[48] The abnormal phenomenon in achieving larger direct band gap and stronger PL emission on such folded MoS_2 layers can be attributed to weak interlayer coupling and compressive strain using the PCF strategy. To further analyze the dependence of PL enhancement on compressive strain, the PL intensity is estimated via the following formulas[49]

$$\mathrm{PL} \propto [\eta_{\mathrm{int}} \times n_{\mathrm{d}}] \quad (4)$$

$$\eta_{\mathrm{int}} = \frac{Xp}{Xp + Yp^2 + Z} \quad (5)$$

where n_{d} is the number of electrons in the conduction band (CB) valley, η_{int} is the internal radiative efficiency of direct transition between the lowest point of the CB and the highest point of the valence band (VB), p represents the majority hole concentration in the VB, and X, Y, and Z are the recombination rate constants for various processes. PL intensity depends on η_{int} and n_{d} when assuming that the rate constants X, Y, and Z to be constant with strain. Upon compressive strain by PCF, the direct gap transition of the MoS_2 is broadened, leading to an increased internal radiative efficiency of direct transition η_{int} compared to indirect transition.[47] On the other hand, the folded bilayer has a much larger interlamellar spacing compared to the intrinsic bilayer, corresponding to an extremely weakly coupled superposition of two monolayer MoS_2 and a dramatically slower electronic relaxation.[50] As a result, the number of electrons n_{d} in the direct CB valley is increased, and the overall PL intensity of folded MoS_2 by PCF is obviously enhanced.

Broadening Electronic Band Gap of Folded MoS_2 Using the PCF Strategy. The evolution of band gap increase as a function of strain was systematically studied on folded structures by PCF (Figure 4a,b). By analyzing SAED patterns of each folded MoS_2, the compressive strains can be extracted. The thermal engineering under different temperature differences (25, 30, 35 and 40 °C) led to a monotonic increase in compressive strains and controllably realized compressive strains ranging from 0.2 to 1.3%. The dependences of characteristic peaks in Raman and PL on strains present a monotonically increasing trend with the increased strains, suggesting that the band gap increase in folded MoS_2 can be controlled via the thermal engineering of paraffin during PCF. By further tuning the paraffin with higher thermal expansion coefficients, larger compressive strain can be achieved.

To explore the origin of optical band gap increase on the folded MoS_2, density functional theory (DFT) simulations were performed on monolayer MoS_2 with biaxial compressive strain in the 0.2–1.3% range by considering the paraffin thickness, type, and temperature gradient. As shown in Figure

https://doi.org/10.1021/acsami.1c11269
ACS Appl. Mater. Interfaces 2021, 13, 40922–40931

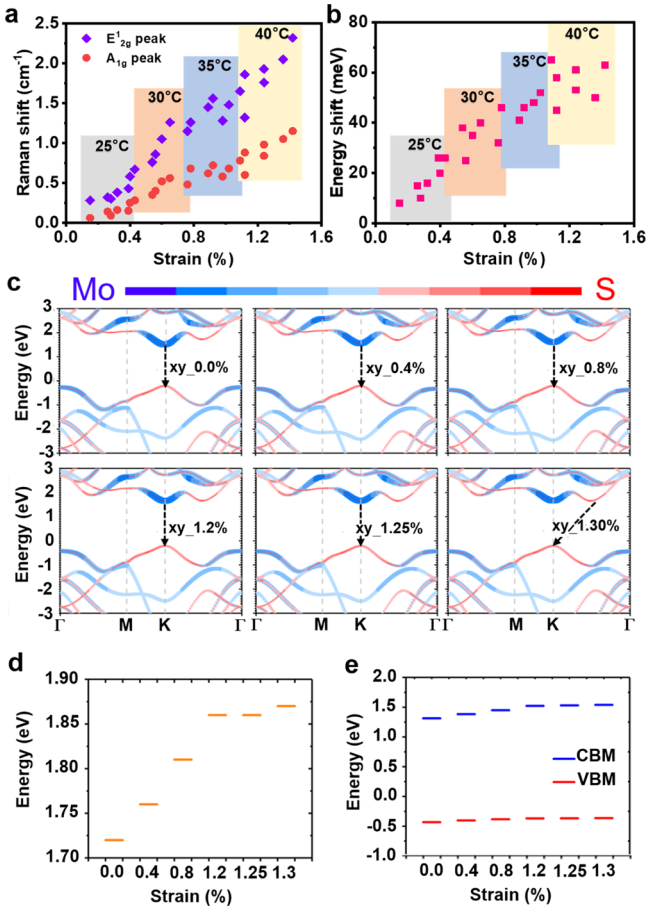

Figure 4. Dependences of band gap increase as a function of strain. (a,b) Dependences of shifts of (a) A_{1g} and E_{2g}^1 in Raman spectra and (b) A exciton peak in PL as a function of compressive strains. (c–e) Calculated electronic properties of (c) band structures, (d) band gap values at K point, and (e) positions of the VBM and CBM of the MoS_2 monolayer compared with the vacuum level at K point depending on biaxial compressive strain at the values of 0, 0.4, 0.8, 1.2, 1.25, and 1.3%.

4c, the electronic band gap remains direct and progressively increases from 1.72 eV in the strain-free sample to 1.86 eV at the 1.25% compressive strain (Table S2, Supporting Information). Though the band gap slightly underestimates compared to experimental values due to the self-interaction error of the Perdew–Burke–Ernzerhof (PBE) function,[51] a self-interaction correction to density functional approximation for many-electron systems, the obtained results are consistent with PL experiments. Both the valence band maximum (VBM) and conduction band minimum (CBM) move to higher energies upon increasing compressive strain, presumably leading to increase on both on and off current in transistors (Figure 4e). The 1.3% biaxial compressive strain is beyond the maximum strain value measured on our samples, which makes the band gap convert into indirect ones and decreases the PL intensity. Calculated values of band gap versus compressive strain are plotted in Figure 4d. The largest band gap of folded MoS_2 by our PCF strategy is ~1.90 meV at room temperature, and this is the largest direct band gap of MoS_2 reported so far (Table S3, Supporting Information).

Optoelectronic Applications of Folded MoS_2 Using the PCF Strategy. Successful creation of folded MoS_2 with larger band gap and enhanced PL on any substrate immediately allowed us to fabricate FETs and photodetectors with better performance, such as higher mobility and photoresponsivity. We fabricated FETs on folded and unfolded regions with bottom gates and top source/drain contacts on SiO_2/Si substrates (Figure S15, Supporting Information), and compared their photoresponses under 532 nm light at different illumination power intensity (Figure 5a). Representative transfer curves showed typical n-type behavior (Figure 5b). Output curves demonstrated ohmic-like contacts under low voltage bias (Figure 5c). Based on the statistical analysis of 30 FETs (Figure 5d,e), mobility of folded bilayer, intrinsic bilayer, and unfolded monolayer MoS_2 is 32.4 ± 4.7 $cm^2/(V\ s)$, 24.3 ± 4.1 $cm^2/(V\ s)$, and 16.5 ± 2.2 $cm^2/(V\ s)$, and carrier density is (3.2 ± 0.4) × 10^{12} cm^{-2}, (2.7 ± 0.4) × 10^{12} cm^{-2}, and (2.4 ± 0.2) × 10^{12} cm^{-2}, respectively, at V_{ds} = 1 V and V_{gs} = 30 V. Values for unfolded monolayer MoS_2 are consistent with most reports of pristine monolayer.[8] The increased values of mobility, electron density, and on/off ratio of folded bilayer MoS_2 can be attributed to the larger band gap induced by compressive strain and weak interlayer coupling generated during the PCF process. On the other hand, according to the PL intensity, the number of electrons n_d of folded MoS_2 by PCF in the direct CB valley is obviously increased (Figure 5f). Taken together, the electrical properties of folded bilayer MoS_2 were superior to those of intrinsic bilayer and unfolded monolayer MoS_2.

Upon light illumination, both folded and unfolded MoS_2 exhibited positive photoresponses, and the drain current increased when the light power intensity increased (Figure 5g,h). Photoresponsivity versus power density of folded and unfolded MoS_2 were compared and are shown in Figure 5i under 532 nm light at V_{ds} = 1 V and V_{gs} = 0 V. It showed that photoresponsivity of folded MoS_2 was almost 20-fold than that of unfolded MoS_2 respectively. The large photoresponsivity of folded MoS_2 is mainly due to the enhancement of light absorption, which can be revealed from the stronger intensity of PL spectra. Based on above demonstrations, we concluded that the folded multilayer using the PCF strategy can result in better optoelectronic performance, such as almost double higher mobility, 1.3 times higher electron density, and 20 times larger photoresponsivity.

CONCLUSIONS

In summary, we demonstrated a PCF strategy to achieve folded multilayer 2D materials with controllable broadening of electronic band gap on any substrate. Compared with most strain engineering methods, folded multilayer MoS_2 using the PCF strategy showed unique blue-shifts and stiffening for in-plane Raman vibration modes and direct gap transition of PL peaks, suggesting larger band gap, reduced interlayer coupling, and increased carrier density. Preliminary applications of FETs and photodetectors proved these advantages, demonstrating almost double higher mobility, 1.3 times higher carrier density, and 20 times larger photoresponsivity on folded multilayer MoS_2 using the PCF strategy. In addition, we have extended our strategy to other 2D materials. We believe our PCF strategy, as an efficient way to widen electronic band gap with long-lasting, transferability, and controllability, will pave a new way toward optoelectronic applications of 2D materials.

EXPERIMENTAL SECTION

Paraffin-Assisted Transfer. To prepare the paraffin solution, paraffin pastilles were pre-baked at 80 °C for 1 min. Paraffin solution

https://doi.org/10.1021/acsami.1c11269
ACS Appl. Mater. Interfaces 2021, 13, 40922–40931

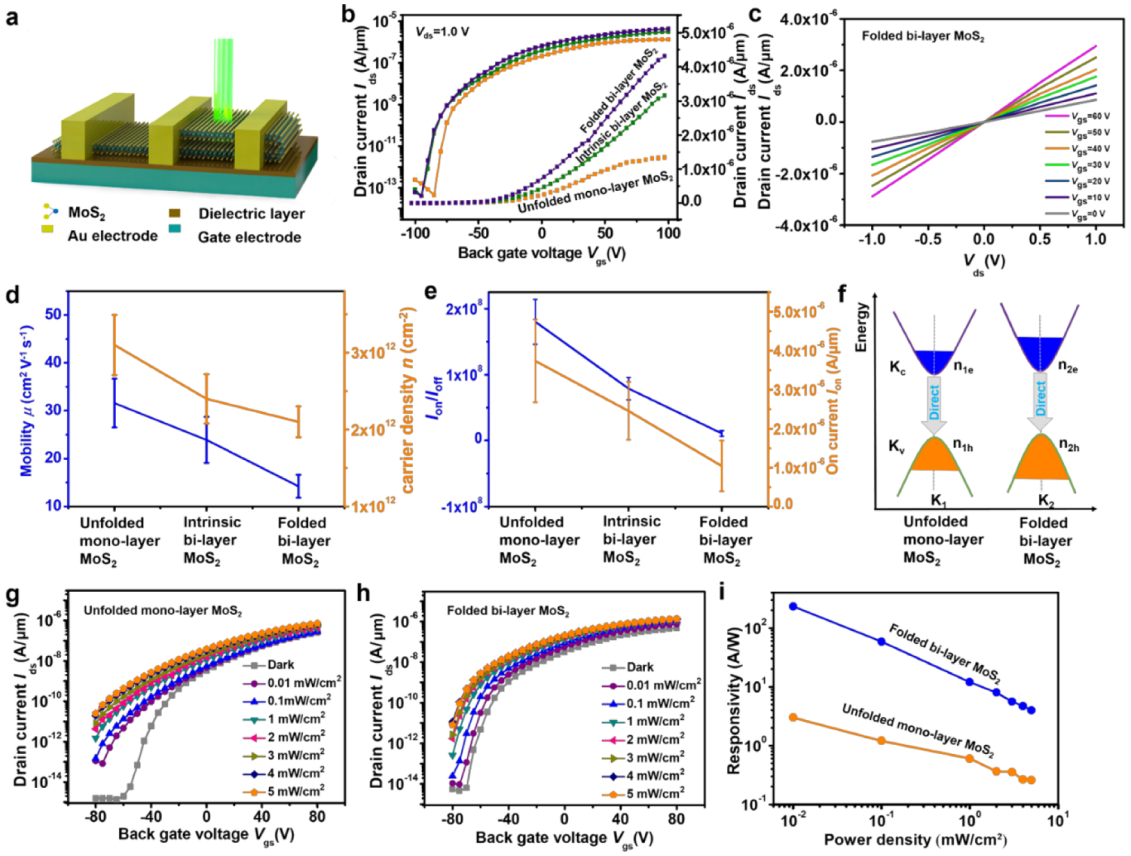

Figure 5. Optoelectronic applications of folded MoS_2 using the PCF strategy. (a) Schematic diagram of the FETs and photodetectors of folded MoS_2 using the PCF strategy. (b) Transfer characteristics of unfolded and folded MoS_2. (c) Output characteristics of folded MoS_2. (d,e) Mobility μ, carrier density n (d), and I_{on}/I_{off}, on current I_{on} (e) of unfolded monolayer, intrinsic bilayer, and folded bilayer MoS_2. (f) Schematic diagram explaining the enhancement in electrical properties after the PCF strategy. (g,h) Transfer characteristics of (g) unfolded and (h) folded MoS_2 upon 532 nm light illumination with power density ranging from 0 to 5 mW/cm^2. (i) Responsivity vs power density of unfolded and folded MoS_2 at V_{ds} = 1 V and V_{gs} = 0 V.

was drop-coated on a sample (i.e., CVD MoS_2 synthesized on a SiO_2/Si substrate), which would solidify in less than 1 min at room temperature. The paraffin-covered MoS_2 on the SiO_2/Si substrate was then placed on a spin coater to achieve a uniform and thinner coverage of the paraffin film. A heat gun was used to blow on the sample, making the paraffin melt again. Once the paraffin turned into the liquid form, the sample was spun at 1000 rpm for 2 min with continuous heat gun blowing. After spin-coating, the sample was immersed in the KOH solution at 45 °C for 6 h, followed by soaking in deionized water at the same temperature to remove KOH. Then, the sample on deionized water was kept at the 5 °C (or 10, 15, and 20 °C) for at least 24 h. The destination substrate (i.e., SiO_2/Si substrate) was used to scoop the paraffin-supported MoS_2 film from the deionized water. After that, the sample was kept at 5 °C (or 10, 15, and 20 °C) in a refrigerator for air drying more than 8 h to minimize the residual water. Finally, the paraffin support layer was removed using hexane solution for 2 h, leaving MoS_2 on the destination substrate.

CVD Growth of 2D Monolayers. Single-crystalline MoS_2 and $MoSe_2$ were grown in a two temperature-zone tubular furnace at a low pressure. For CVD growth of MoS_2, sulfur powder (1.5 g) area of the furnace was heated to 190 °C; in the meanwhile, the Mo source (oxidized molybdenum foil) area was heated to 830 °C within 30 min at a carrier gas flow of 100 sccm Ar. For CVD growth of $MoSe_2$, 50 mg of selenium pills and 0.3 mg of MoO_3 were used as Se and Mo precursors, respectively. MoO_3 area of the furnace was heated to 750 °C within 18 min, while Se area was heated to 340 °C at the same time at a carrier gas flow of 20 sccm Ar and 5 sccm H_2.

h-BN and graphene were synthesized in a single-temperature-zone tubular furnace under atmospheric pressure. Cu foils were first polished and loaded into the center of the heating zone. For CVD growth of h-BN, the temperature of the heating zone was ramped to 1000 °C within 60 min, with a carrier gas flow of 200 sccm Ar and 50 sccm H_2. Then, ammonia borane placed in a mini-tube at upstream as a BN precursor was heated to 85 °C for 10 min. For CVD growth of graphene, the Cu foil was exposed in a mixed gas with a constant flow rate of 20 sccm H_2 and 100 sccm CH_4 for 40 min at 1000 °C.

Characterization. Raman spectra, PL spectra, and imaging were measured by a confocal Raman microscope (HORRIBA, LabRAM HR 800) with a 532 nm laser. The laser power was maintained at 100 μW. The reflectance contrast spectra were measured on SiO_2/Si substrates under the conditions of 100 grating, ×100 objective, and 25 hole (HR_HORIBA). $\Delta R/R$ was collected via the equation: $\Delta R/R = R_{sample} - R_{SiO_2}/R_{SiO_2}$. Here, R_{SiO_2} and R_{sample} are the reflectance of the bare SiO_2/Si substrate and the sample on the SiO_2/Si substrate, and ΔR is the difference between them. Optical microscopy images were captured by Leica DM2700M. AFM images were obtained using a Digital Instrument Multimode Nanoscope IIIA in the tapping mode. SEM images were taken using a Hitachi SU8010. Transmission electron microscopy imaging was performed by a FEI Tecnai TF20 (Philip).

Fabrication and Measurements of MoS_2 FETs and Photodetectors. Folded bilayer and unfolded monolayer MoS_2 on a SiO_2/Si substrate were used to fabricate back-gated FETs. The sample was first spin-coated with a 500 nm thick layer of methylmethacrylate (MMA) (Allresist: AR-P 672.02) and poly-methylmethacrylate (PMMA) (MicroChem: EL6). The MMA layer was baked at 150 °C for 2 min, and the PMMA layer was baked at 175 °C for 2 min. Then, the source/drain contacts were defined using electron beam

https://doi.org/10.1021/acsami.1c11269
ACS Appl. Mater. Interfaces 2021, 13, 40922−40931

lithography and metallized with 3/50 nm of Cr/Au using thermal evaporation, followed by a 4 h lift-off process in acetone at 60 °C. Finally, these devices were annealed at 100 °C for 1 h under an N_2 atmosphere to reduce the contact resistance between channel and metal electrodes. FETs were measured in air using Keithley 2636b. Linear field effect mobility (μ) and carrier density (n) were calculated by following formulas[52]

$$\mu = \frac{L_{ch}}{C_{OX}V_{ds}W_{ch}} \times \frac{dI_{ds}}{dI_{gs}} \quad (6)$$

$$n = \frac{L_{ch}I_{ds}}{e\mu W_{ch}V_{ds}} \quad (7)$$

where C_{OX} is the gate capacitance (1.35×10^{-8} F cm^{-2} for 300 nm thick SiO_2), L_{ch} and W_{ch} are the channel length and width, respectively, and e is the electron charge (1.6×10^{-19} C).

In order to characterize the photoelectrical properties of FETs, three-terminal measurement was performed under 532 nm light with an illuminance area of 1 cm^2 and power densities of 0.01, 0.1, 1, 2, 3, 4, and 5 mW cm^{-2}. We calculated photoresponsivity (R) via the following formula[52]

$$R = \frac{I_{ph}}{P_{in}} \quad (8)$$

where I_{ph} is the photocurrent, I_{dark} is the dark current, and P_{in} is the power density of light.

3D Field Effect Simulation. A 3D field effect model was developed to better understand the process of paraffin-enabled wrinkled/folded MoS_2. The simulation was performed using ANSYS R 2019 R2 software. Young's modulus, Poisson's ratio, and coefficient of thermal expansion were used in the simulation. The discretized field effect models contain about 719,336 nodes and 170,409 elements.

DFT Calculations. To investigate the electronic band gap change depending on external compressive strain, a monolayer MoS_2 unit cell with a lattice constant of 3.169 Å is chosen to represent a strain-free sample. By varying cell parameters to 3.156, 3.144, 3.131, 3.129, and 3.128 Å, five strained MoS_2 slabs are obtained at the biaxial compressive strain of 0.4, 0.8, 1.2, 1.25, and 1.30%, respectively. The MoS_2 slabs are separated from their periodic images along the surface normal by a vacuum region of 15 Å. Geometric optimization and electronic structure calculations are calculated with the Vienna Ab initio Simulation Package (VASP)[53,54] using the PBE exchange–correlation functional[55] and projected-augmented wave pseudopotentials[56] for the valence and core electrons. The energy cutoff is 400 eV. The optimizations are carried out with the $9 \times 9 \times 1$ k-point Monhorst-Pack mesh.[57] Then, band structure calculations are performed using the line-mode approach along the Γ–M–K–Γ path with 50 k-points between two adjacent high-symmetric k-points.

■ ASSOCIATED CONTENT

Supporting Information

The Supporting Information is available free of charge at https://pubs.acs.org/doi/10.1021/acsami.1c11269.

SEM image of folded tri-layer MoS_2; folded bilayer MoS_2 on the rigid and elastomeric substrates; universality of the PCF strategy; field effect simulation of the compressive folding; optical microscopy images of different folded structures, statistical folded areas, different thicknesses paraffin, CVD-grown monolayer and bilayer MoS_2, and devices based on monolayer and folded bilayer MoS_2; temperature-dependent investigation, position mapping, and intensity evolution of PL spectra of folded bilayer MoS_2; SAED patterns of unfolded monolayer and folded bilayer MoS_2; DFT calculated values for monolayer MoS_2; and comparisons of fabrication of topological 2D materials and strain engineering methods (PDF)

■ AUTHOR INFORMATION

Corresponding Author

Nan Liu − *Beijing Key Laboratory of Energy Conversion and Storage Materials, College of Chemistry, Beijing Normal University, Beijing 100875, P. R. China;* orcid.org/0000-0002-1793-7372; Email: nanliu@bnu.edu.cn

Authors

Weifeng Zhang − *Beijing Key Laboratory of Energy Conversion and Storage Materials, College of Chemistry, Beijing Normal University, Beijing 100875, P. R. China*

Zihan Zhao − *Beijing Key Laboratory of Energy Conversion and Storage Materials, College of Chemistry, Beijing Normal University, Beijing 100875, P. R. China; School of Chemistry and Chemical Engineering, Shihezi University, Shihezi, Xinjiang 832003, China*

Yating Yang − *Beijing Key Laboratory of Energy Conversion and Storage Materials, College of Chemistry, Beijing Normal University, Beijing 100875, P. R. China*

Yan Zhang − *Beijing Key Laboratory of Energy Conversion and Storage Materials, College of Chemistry, Beijing Normal University, Beijing 100875, P. R. China*

He Hao − *Beijing Key Laboratory of Energy Conversion and Storage Materials, College of Chemistry, Beijing Normal University, Beijing 100875, P. R. China*

Li Li − *School of Chemistry and Chemical Engineering, Nanjing University, Nanjing 210093, China*

Weigao Xu − *School of Chemistry and Chemical Engineering, Nanjing University, Nanjing 210093, China;* orcid.org/0000-0002-3014-756X

Banghua Peng − *School of Chemistry and Chemical Engineering, Shihezi University, Shihezi, Xinjiang 832003, China*

Run Long − *Beijing Key Laboratory of Energy Conversion and Storage Materials, College of Chemistry, Beijing Normal University, Beijing 100875, P. R. China;* orcid.org/0000-0003-3912-8899

Complete contact information is available at: https://pubs.acs.org/10.1021/acsami.1c11269

Author Contributions

‖W.Z. and Z.Z. contributed equally to this work.

Notes

The authors declare no competing financial interest.

■ ACKNOWLEDGMENTS

This research is supported by the National Natural Science Foundation of China (21903007 and 22072006), Young Thousand Talents Program (110532103), Beijing Normal University Startup funding (312232102), Beijing Municipal Science & Technology Commission (no. Z191100000819002), and the Fundamental Research Funds for the Central Universities (310421109).

■ REFERENCES

(1) Zeng, M.; Liu, J.; Zhou, L.; Mendes, R. G.; Dong, Y.; Zhang, M.-Y.; Cui, Z.-H.; Cai, Z.; Zhang, Z.; Zhu, D.; Yang, T.; Li, X.; Wang, J.; Zhao, L.; Chen, G.; Jiang, H.; Rümmeli, M. H.; Zhou, H.; Fu, L.

Bandgap Tuning of Two-Dimensional Materials by Sphere Diameter Engineering. *Nat. Mater.* **2020**, *19*, 528−533.
(2) Pak, S.; Lee, J.; Jang, A. R.; Kim, S.; Park, K. H.; Sohn, J. I.; Cha, S. Strain-Engineering of Contact Energy Barriers and Photoresponse Behaviors in Monolayer MoS_2 Flexible Devices. *Adv. Funct. Mater.* **2020**, *30*, 2002023.
(3) Wang, Q. H.; Kalantar-Zadeh, K.; Kis, A.; Coleman, J. N.; Strano, M. S. Electronics and Optoelectronics of Two-Dimensional Transition Metal Dichalcogenides. *Nat. Nanotechnol.* **2012**, *7*, 699−712.
(4) Ricciardulli, A. G.; Blom, P. W. M. Solution−Processable 2D Materials Applied in Light−Emitting Diodes and Solar Cells. *Adv. Mater. Technol.* **2020**, *5*, 1900972.
(5) Deng, D.; Novoselov, K. S.; Fu, Q.; Zheng, N.; Tian, Z.; Bao, X. Catalysis with Two-Dimensional Materials and Their Heterostructures. *Nat. Nanotechnol.* **2016**, *11*, 218−230.
(6) Bhimanapati, G. R.; Lin, Z.; Meunier, V.; Jung, Y.; Cha, J.; Das, S.; Xiao, D.; Son, Y.; Strano, M. S.; Cooper, V. R.; Liang, L.; Louie, S. G.; Ringe, E.; Zhou, W.; Kim, S. S.; Naik, R. R.; Sumpter, B. G.; Terrones, H.; Xia, F.; Wang, Y.; Zhu, J.; Akinwande, D.; Alem, N.; Schuller, J. A.; Schaak, R. E.; Terrones, M.; Robinson, J. A. Recent Advances in Two-Dimensional Materials beyond Graphene. *ACS Nano* **2015**, *9*, 11509−11539.
(7) Anasori, B.; Lukatskaya, M. R.; Gogotsi, Y. 2D Metal Carbides and Nitrides (MXenes) for Energy Storage. *Nat. Rev. Mater.* **2017**, *2*, 16098.
(8) Cai, Z.; Liu, B.; Zou, X.; Cheng, H.-M. Chemical Vapor Deposition Growth and Applications of Two−Dimensional Materials and Their Heterostructures. *Chem. Rev.* **2018**, *118*, 6091−6133.
(9) Xiong, Q. Two-Dimensional Materials: New Opportunities for Electronics, Photonics and Optoelectronics. *Sci. Bull.* **2019**, *64*, 1031−1032.
(10) Kappera, R.; Voiry, D.; Yalcin, S. E.; Branch, B.; Gupta, G.; Mohite, A. D.; Chhowalla, M. Phase-Engineered Low-Resistance Contacts for Ultrathin MoS_2 Transistors. *Nat. Mater.* **2014**, *13*, 1128−1134.
(11) Luo, P.; Zhuge, F.; Zhang, Q.; Chen, Y.; Lv, L.; Huang, Y.; Li, H.; Zhai, T. Doping Engineering and Functionalization of Two-Dimensional Metal Chalcogenides. *Nanoscale Horiz.* **2019**, *4*, 26−51.
(12) Zhang, W.; Zhang, Y.; Qiu, J.; Zhao, Z.; Liu, N. Topological Structures of Transition Metal Dichalcogenides: A Review on Fabrication, Effects, Application, and Potential. *InfoMat* **2021**, *3*, 133−154.
(13) Crowne, F. J.; Amani, M.; Birdwell, A. G.; Chin, M. L.; O'Regan, T. P.; Najmaei, S.; Liu, Z.; Ajayan, P. M.; Lou, J.; Dubey, M. Blueshift of the A-Exciton Peak in Folded Monolayer 1H-MoS_2. *Phys. Rev. B: Condens. Matter Mater. Phys.* **2013**, *88*, 235302.
(14) Cui, X.; Kong, Z.; Gao, E.; Huang, D.; Hao, Y.; Shen, H.; Di, C.-an; Xu, Z.; Zheng, J.; Zhu, D. Rolling Up Transition Metal Dichalcogenide Nanoscrolls via One Drop of Ethanol. *Nat. Commun.* **2018**, *9*, 1301.
(15) Castellanos-Gomez, A.; van der Zant, H. S. J.; Steele, G. A. Folded MoS_2 Layers with Reduced Interlayer Coupling. *Nano Res.* **2014**, *7*, 572−578.
(16) Kim, K.; Lee, Z.; Malone, B. D.; Chan, K. T.; Alemán, B.; Regan, W.; Gannett, W.; Crommie, M. F.; Cohen, M. L.; Zettl, A. Multiply Folded Graphene. *Phys. Rev. B: Condens. Matter Mater. Phys.* **2011**, *83*, 245433.
(17) Zang, J.; Ryu, S.; Pugno, N.; Wang, Q.; Tu, Q.; Buehler, M. J.; Zhao, X. Multifunctionality and Control of the Crumpling and Unfolding of Large-Area Graphene. *Nat. Mater.* **2013**, *12*, 321−325.
(18) Guo, Y.; Guo, W. Electronic and Field Emission Properties of Wrinkled Graphene. *J. Mater. Chem. C* **2013**, *117*, 692−696.
(19) Deng, S.; Gao, E.; Wang, Y.; Sen, S.; Sreenivasan, S. T.; Behura, S.; Král, P.; Xu, Z.; Berry, V. Confined, Oriented, and Electrically Anisotropic Graphene Wrinkles on Bacteria. *ACS Nano* **2016**, *10*, 8403−8412.
(20) Deng, S.; Che, S.; Debbarma, R.; Berry, V. Strain in a Single Wrinkle on an MoS_2 Flake for In-Plane Realignment of Band Structure for Enhanced Photo-Response. *Nanoscale* **2019**, *11*, 504−511.
(21) Conley, H. J.; Wang, B.; Ziegler, J. I.; Haglund, S. T., Jr.; Bolotin, K. I.; Bolotin, K. I. Band-Gap Engineering of Strained Monolayer and Bilayer MoS_2. *Nano Lett.* **2013**, *13*, 3626−3630.
(22) Plechinger, G.; Castellanos-Gomez, A.; Buscema, M.; van der Zant, H. S. J.; Steele, G. A.; Kuc, A.; Heine, T.; Schüller, C.; Korn, T. Control of Biaxial Strain in Single-Layer Molybdenite Using Local Thermal Expansion of the Substrate. *2D Mater* **2015**, *2*, 015006.
(23) Kim, S. J.; Kwon, O.; Kim, D. W.; Kim, J.; Jung, H.-T. Influence of Graphene Thickness and Grain Boundaries on MoS_2 Wrinkle Nanostructures. *Phys. Chem. Chem. Phys.* **2018**, *20*, 17000−17008.
(24) Castellanos-Gomez, A.; Roldán, R.; Cappelluti, E.; Buscema, M.; Guinea, F.; van der Zant, H. S. J.; Steele, G. A. Local Strain Engineering in Atomically Thin MoS_2. *Nano Lett.* **2013**, *13*, 5361−5366.
(25) Zhao, J.; Deng, Q.; Ly, T. H.; Han, G. H.; Sandeep, G.; Rümmeli, M. H. Two-Dimensional Membrane as Elastic Shell with Proof on the Folds Revealed by Three-Dimensional Atomic Mapping. *Nat. Commun.* **2015**, *6*, 8935.
(26) Hui, Y. Y.; Liu, X.; Jie, W.; Chan, N. Y.; Hao, J.; Hsu, Y.-T.; Li, L.-J.; Guo, W.; Lau, S. P. Exceptional Tunability of Band Energy in a Compressively Strained Trilayer MoS_2 Sheet. *ACS Nano* **2013**, *7*, 7126−7131.
(27) Radisavljevic, B.; Radenovic, A.; Brivio, J.; Giacometti, V.; Kis, A. Single-Layer MoS_2 Transistors. *Nat. Nanotechnol.* **2011**, *6*, 147−150.
(28) Butler, S. Z.; Hollen, S. M.; Cao, L.; Cui, Y.; Gupta, J. A.; Gutiérrez, H. R.; Heinz, T. F.; Hong, S. S.; Huang, J.; Ismach, A. F.; Johnston-Halperin, E.; Kuno, M.; Plashnitsa, V. V.; Robinson, R. D.; Ruoff, R. S.; Salahuddin, S.; Shan, J.; Shi, L.; Spencer, M. G.; Terrones, M.; Windl, W.; Goldberger, J. E. Progress, Challenges, and Opportunities in Two-Dimensional Materials beyond Graphene. *ACS Nano* **2013**, *7*, 2898−2926.
(29) Choi, G. J.; Van Le, Q.; Choi, K. S.; Kwon, K. C.; Jang, H. W.; Gwag, J. S.; Kim, S. Y. Polarized Light−Emitting Diodes Based on Patterned MoS_2 Nanosheet Hole Transport Layer. *Adv. Mater.* **2017**, *29*, 1702598.
(30) Yang, W.; Shang, J.; Wang, J.; Shen, X.; Cao, B.; Peimyoo, N.; Zou, C.; Chen, Y.; Wang, Y.; Cong, C.; Huang, W.; Yu, T. Electrically Tunable Valley-Light Emitting Diode (vLED) Based on CVD-Grown Monolayer WS_2. *Nano Lett.* **2016**, *16*, 1560−1567.
(31) Wang, J.; Guo, X.; Yu, Z.; Ma, Z.; Liu, Y.; Lin, Z.; Chan, M.; Zhu, Y.; Wang, X.; Chai, Y. Low-Power Complementary Inverter with Negative Capacitance 2D Semiconductor Transistors. *Adv. Funct. Mater.* **2020**, *30*, 2003859.
(32) Liu, E.; Fu, Y.; Wang, Y.; Feng, Y.; Liu, H.; Wan, X.; Zhou, W.; Wang, B.; Shao, L.; Ho, C.-H.; Huang, Y.-S.; Cao, Z.; Wang, L.; Li, A.; Zeng, J.; Song, F.; Wang, X.; Shi, Y.; Yuan, H.; Hwang, H. Y.; Cui, Y.; Miao, F.; Xing, D. Integrated Digital Inverters Based on Two-Dimensional Anisotropic ReS_2 Field-Effect Transistors. *Nat. Commun.* **2015**, *6*, 6991.
(33) Shin, Y. S.; Lee, K.; Duong, D. L.; Kim, J. S.; Kang, W. T.; Kim, J. E.; Won, U. Y.; Lee, I.; Lee, H.; Heo, J.; Lee, Y. H.; Yu, W. J. Li Intercalation Effects on Interface Resistances of High-Speed and Low-Power WSe_2 Field-Effect Transistors. *Adv. Funct. Mater.* **2020**, *30*, 2003688.
(34) Rathi, S.; Lee, I.; Lim, D.; Wang, J.; Ochiai, Y.; Aoki, N.; Watanabe, K.; Taniguchi, T.; Lee, G.-H.; Yu, Y.-J.; Kim, P.; Kim, G.-H. Tunable Electrical and Optical Characteristics in Monolayer Graphene and Few-Layer MoS_2 Heterostructure Devices. *Nano Lett.* **2015**, *15*, 5017−5024.
(35) Jo, S.-H.; Kang, D.-H.; Shim, J.; Jeon, J.; Jeon, M. H.; Yoo, G.; Kim, J.; Lee, J.; Yeom, G. Y.; Lee, S.; Yu, H.-Y.; Choi, C.; Park, J.-H. A High-Performance WSe_2/h-BN Photodetector Using a Triphenylphosphine (PPh_3)-Based n-Doping Technique. *Adv. Mater.* **2016**, *28*, 4824−4831.

https://doi.org/10.1021/acsami.1c11269
ACS Appl. Mater. Interfaces 2021, 13, 40922−40931

(36) Lopez-Sanchez, O.; Lembke, D.; Kayci, M.; Radenovic, A.; Kis, A. Ultrasensitive Photodetectors Based on Monolayer MoS_2. *Nat. Nanotechnol.* **2013**, *8*, 497−501.
(37) Yang, S.; Wang, C.; Sahin, H.; Chen, H.; Li, Y.; Li, S.-S.; Suslu, A.; Peeters, F. M.; Liu, Q.; Li, J.; Tongay, S. Tuning the Optical, Magnetic, and Electrical Properties of $ReSe_2$ by Nanoscale Strain Engineering. *Nano Lett.* **2015**, *15*, 1660−1666.
(38) Kato, E. Brillouin Scattering in Polymethyl Methacrylate from 4 to 300 K: Temperature Dependence of the Grüneisen Constant and Thermal Properties. *J. Chem. Phys.* **1980**, *73*, 1020.
(39) Leong, W. S.; Wang, H.; Yeo, J.; Martin-Martinez, F. J.; Zubair, A.; Shen, P.-C.; Mao, Y.; Palacios, T.; Buehler, M. J.; Hong, J.-Y.; Kong, J. Paraffin-Enabled Graphene Transfer. *Nat. Commun.* **2019**, *10*, 867.
(40) Liu, R.; Bonanno, J.; Yang, J.; Lenigk, R.; Grodzinski, P. Single-Use, Thermally Actuated Paraffin Valves for Microfluidic Applications. *Sens. Actuators, B* **2004**, *98*, 328−336.
(41) Yang, P.; Zou, X.; Zhang, Z.; Hong, M.; Shi, J.; Chen, S.; Shu, J.; Zhao, L.; Jiang, S.; Zhou, X.; Huan, Y.; Xie, C.; Gao, P.; Chen, Q.; Zhang, Q.; Liu, Z.; Zhang, Y. Batch Production of 6-Inch Uniform Monolayer Molybdenum Disulfide Catalyzed by Sodium in Glass. *Nat. Commun.* **2018**, *9*, 979.
(42) Ohashi, M.; Paffenbarger, G. C. Melting, Flow, and Thermal Expansion Characteristics of Some Dental and Commercial Waxes. *J. Am. Dent. Assoc.* **1966**, *72*, 1141−1150.
(43) Ruppert, C.; Aslan, O. B.; Heinz, T. F. Optical Properties and Band Gap of Single- and Few-Layer $MoTe_2$ Crystals. *Nano Lett.* **2014**, *14*, 6231−6236.
(44) Paradisanos, I.; McCreary, K. M.; Adinehloo, D.; Mouchliadis, L.; Robinson, J. T.; Chuang, H.-J.; Hanbicki, A. T.; Perebeinos, V.; Jonker, B. T.; Stratakis, E.; Kioseoglou, G. Prominent Room Temperature Valley Polarization in WS_2/Graphene Heterostructures Grown by Chemical Vapor Deposition. *Appl. Phys. Lett.* **2020**, *116*, 203102.
(45) Zhao, W.; Ribeiro, R. M.; Toh, M.; Carvalho, A.; Kloc, C.; Castro Neto, A. H.; Eda, G. Origin of Indirect Optical Transitions in Few-Layer MoS_2, WS_2, and WSe_2. *Nano Lett.* **2013**, *13*, 5627−5634.
(46) Christiansen, D.; Selig, M.; Berghäuser, G.; Schmidt, R.; Niehues, I.; Schneider, R.; Arora, A.; de Vasconcellos, S. M.; Bratschitsch, R.; Malic, E.; Knorr, A. Phonon Sidebands in Monolayer Transition Metal Dichalcogenides. *Phys. Rev. Lett.* **2017**, *119*, 187402.
(47) Jiang, T.; Liu, H.; Huang, D.; Zhang, S.; Li, Y.; Gong, X.; Shen, Y.-R.; Liu, W.-T.; Wu, S. Valley and Band Structure Engineering of Folded MoS_2 Bilayers. *Nat. Nanotechnol.* **2014**, *9*, 825−829.
(48) Mak, K. F.; He, K.; Lee, C.; Lee, G. H.; Hone, J.; Heinz, T. F.; Shan, J. Tightly Bound Trions in Monolayer MoS_2. *Nat. Mater.* **2012**, *12*, 207−211.
(49) Desai, S. B.; Seol, G.; Kang, J. S.; Fang, H.; Battaglia, C.; Kapadia, R.; Ager, J. W.; Guo, J.; Javey, A. Strain-Induced Indirect to Direct Bandgap Transition in Multilayer WSe_2. *Nano Lett.* **2014**, *14*, 4592−4597.
(50) Splendiani, A.; Sun, L.; Zhang, Y.; Li, T.; Kim, J.; Chim, C.-Y.; Galli, G.; Wang, F. Emerging Photoluminescence in Monolayer MoS_2. *Nano Lett.* **2010**, *10*, 1271−1275.
(51) Perdew, J. P.; Zunger, A. Self-Interaction Correction to Density-Functional Approximations for Many-Electron Systems. *Phys. Rev. B: Condens. Matter Mater. Phys.* **1996**, *23*, 5048−5079.
(52) Xie, Y.; Zhang, B.; Wang, S.; Wang, D.; Wang, A.; Wang, Z.; Yu, H.; Zhang, H.; Chen, Y.; Zhao, M.; Huang, B.; Mei, L.; Wang, J. Ultrabroadband MoS_2 Photodetector with Spectral Response from 445 to 2717 nm. *Adv. Mater.* **2017**, *29*, 1605972.
(53) Kresse, G.; Hafner, J. Ab Initio Molecular Dynamics for Liquid Metals. *Phys. Rev. B: Condens. Matter Mater. Phys.* **1993**, *47*, 558−561.
(54) Kresse, G.; Furthmüller, J. Efficient Iterative Schemes for Ab Initio Total-Energy Calculations Using a Plane-Wave Basis Set. *Phys. Rev. B: Condens. Matter Mater. Phys.* **1996**, *54*, 11169−11186.
(55) Perdew, J. P.; Burke, K.; Ernzerhof, M. Generalized Gradient Approximation Made Simple. *Phys. Rev. Lett.* **1996**, *77*, 3865−3868.
(56) Blöchl, P. E. Projector Augmented-Wave Method. *Phys. Rev. B: Condens. Matter Mater. Phys.* **1994**, *50*, 17953−17979.
(57) Monkhorst, H. J.; Pack, J. D. Special Points for Brillouin-Zone Integrations. *Phys. Rev. B: Solid State* **1976**, *13*, 5188−5192.

https://doi.org/10.1021/acsami.1c11269
ACS Appl. Mater. Interfaces 2021, 13, 40922−40931